Int. J. Heat Mass Transfer. Vol. 32, No. 1, pp. 69–79, 1989
Printed in Great Britain

0017–9310/89 $3.00 + 0.00

Solidification of an aqueous ammonium chloride solution in a rectangular cavity—II. Comparison of predicted and measured results

M. S. CHRISTENSON, W. D. BENNON and F. P. INCROPERA
Heat Transfer Laboratory, School of Mechanical Engineering, Purdue University, West Lafayette, IN 47907, U.S.A.

(*Received* 4 *March* 1988 *and in final form* 8 *June* 1988)

Abstract—Comparisons between experimental and numerical results for solidification of a binary NH_4Cl–H_2O solution in a rectangular cavity are made using a newly developed continuum model. The model predicts key features of the solidification process such as liquidus interface irregularities, remelting and the development and subsequent erosion of a double-diffusive interface. However, due to uncertainties in the available property data base and/or limitations in related model assumptions, good quantitative agreement is not obtained for all of the data.

1. INTRODUCTION

WITH RECOGNITION of the fact that liquid motion in the mushy and melt regions can strongly influence species segregation during solidification of a binary substance, efforts have been made to model the segregation process [1–3]. By prescribing solidification rates, the nature of the interdendritic flow, and local temperature gradients, analytical expressions could be developed for the segregation of solute-rich interdendritic fluids due to thermal contraction. The model was improved by Mehrabian *et al.* [4] and Kou *et al.* [5], who treated the mushy region as a Darcian porous medium and explicitly determined interdendritic flow due to buoyancy, as well as thermal contraction. However, as with previous efforts, solidification rates and temperature gradients were prescribed.

The first attempt to couple solutions to the momentum and energy equations in the mushy region was reported by Fujii *et al.* [6]. However, the mushy region was uncoupled from the solid and melt regions, and the transient progression of planar solidus and liquidus interfaces was arbitrarily prescribed. Although Ridder *et al.* [7] considered coupled two-dimensional flows associated with the mushy and melt regions, the need to prescribe the mushy region size and shape limited applicability of the model. Szekely and Jassal [8] were the first to consider momentum and energy transfer in the solid, mushy and liquid regions of a binary system. However, they did not account for species transfer and hence were unable to predict macrosegregation effects. Species transfer was considered in a subsequent study [9], although the existence of a mushy region was ignored.

In the foregoing models, coupling between the solid, mushy and liquid regions was either ignored or treated by means of a multiple region solution. In such a solution separate conservation equations are solved for each region, and the solutions are coupled by applying boundary conditions to interfaces which are assumed to be smooth. More recently, refs. [10, 11] formulated a continuum model for predicting momentum, energy and species transfer in binary phase change systems. Since the model is based on a single set of conservation equations, which applies to each of the three regions, *explicit* consideration is not given to interface motion or boundary conditions internal to the domain. Solutions are subject only to conditions imposed at external boundaries and are capable of predicting important features such as irregular interface morphology and local remelting.

Despite the considerable interest in developing models for the solidification of binary substances, little has been done to validate such models through quantitative comparisons with experimental results. In this paper, a detailed comparison is made between experimental and predicted results for solidification of an NH_4Cl–H_2O solution in a rectangular cavity. The experimental results are obtained from a companion paper [12], while predictions are based on the continuum model of ref. [10]. In addition, parametric calculations based on the continuum model are used to delineate important features of the solidification process.

2. MODEL FORMULATION

Continuum equations governing the conservation of mass, momentum, energy and species for binary phase change systems have been previously developed [10] and, in two-dimensional Cartesian coordinates, may be expressed as

$$\frac{\partial}{\partial t}(\rho)+\nabla\cdot(\rho\mathbf{V})=0 \qquad (1)$$

NOMENCLATURE

c	specific heat
D	mass diffusion coefficient
f	mass fraction
g	volume fraction or gravitational acceleration
h	enthalpy
H	mold height
k	thermal conductivity
k_p	equilibrium partition ratio
K	permeability
K_o	permeability coefficient
L	mold sidewall spacing
P	pressure or isotropic stress component
t	time
T	temperature
T_m	fusion temperature for $f^\alpha = 0$
u, v	x-, y-direction velocity components
$\mathbf{V}$	velocity vector
x, y	Cartesian coordinates.

Greek symbols

β_S	solutal expansion coefficient
β_T	thermal expansion coefficient
μ	dynamic viscosity
ρ	density.

Subscripts

c	cold boundary
e	eutectic
h	hot boundary
k	phase k
l	liquid
liq	liquidus
o	initial
s	solid.

Superscript

α	constituent α (NH_4Cl).

$$\frac{\partial}{\partial t}(\rho u)+\nabla\cdot(\rho\mathbf{V}u)=\nabla\cdot\left(\mu_l\frac{\rho}{\rho_l}\nabla u\right)-\frac{\mu_l}{K}\frac{\rho}{\rho_l}(u-u_s)-\frac{\partial P}{\partial x} \quad (2)$$

$$\frac{\partial}{\partial t}(\rho v)+\nabla\cdot(\rho\mathbf{V}v)=\nabla\cdot\left(\mu_l\frac{\rho}{\rho_l}\nabla v\right)-\frac{\mu_l}{K}\frac{\rho}{\rho_l}(v-v_s)-\frac{\partial P}{\partial y}+\rho g[\beta_T(T-T_e)+\beta_S(f_l^\alpha-f_{l,e}^\alpha)] \quad (3)$$

$$\frac{\partial}{\partial t}(\rho h)+\nabla\cdot(\rho\mathbf{V}h)=\nabla\cdot\left(\frac{k}{c_s}\nabla h\right)+\nabla\cdot\left[\frac{k}{c_s}\nabla(h_s-h)\right]-\nabla\cdot[\rho(h_l-h)(\mathbf{V}-\mathbf{V}_s)] \quad (4)$$

$$\frac{\partial}{\partial t}(\rho f^\alpha)+\nabla\cdot(\rho\mathbf{V}f^\alpha)=\nabla\cdot(\rho D\nabla f^\alpha)+\nabla\cdot[\rho D\nabla(f_l^\alpha-f^\alpha)]-\nabla\cdot[\rho(f_l^\alpha-f^\alpha)(\mathbf{V}-\mathbf{V}_s)]. \quad (5)$$

The continuum density, velocity, enthalpy and species mass fraction appearing in equations (1)–(5) are defined as

$$\rho = g_s\rho_s+g_l\rho_l \quad (6)$$

$$\mathbf{V} = f_s\mathbf{V}_s+f_l\mathbf{V}_l \quad (7)$$

$$h = f_sh_s+f_lh_l \quad (8)$$

$$f^\alpha = f_sf_s^\alpha+f_lf_l^\alpha. \quad (9)$$

The enthalpy of phase k (k = s, l) is defined as

$$h_k = \int_0^T c_k\,dT+h_k^\circ \quad (10)$$

and the continuum thermal conductivity and mass diffusion coefficient are

$$k = g_sk_s+g_lk_l \quad (11)$$

$$D = f_lD_l^\alpha. \quad (12)$$

The mushy region permeability appearing in the x and y momentum equations is based on the Kozeny–Carman equation [13]

$$K = K_o\left[\frac{g_l^3}{(1-g_l)^2}\right] \quad (13)$$

where K_o is a constant which depends on the specific multiphase region structure.

Linearizing the phase diagram for a binary substance, the solid mass fraction and liquid mass fraction of constituent α may be expressed as

$$f_s = \frac{1}{1-k_p}\left[\frac{T-T_{liq}}{T-T_m}\right] \quad (14)$$

$$f_l^\alpha = \left[\frac{1}{1+f_s(k_p-1)}\right]f^\alpha \quad (15)$$

where T_{liq} is the liquidus temperature corresponding to f^α, T_m the fusion temperature for $f^\alpha \to 0$, and k_p the equilibrium partition ratio (the ratio of the slopes of the liquidus and solidus lines). Values of T_{liq}, T_m and k_p may be obtained from the phase diagram for a particular mixture, while the mixture species composition f^α is obtained from equation (5).

Assumptions inherent in the foregoing model are (i) laminar flow, (ii) Newtonian phase behavior, (iii) local thermodynamic equilibrium, (iv) constant properties, (v) constant density ($\rho_s = \rho_l$) except for variations in the buoyancy force, (vi) Boussinesq approximation, (vii) isotropic permeability, and (viii) negligible species diffusion in the solid phase. The

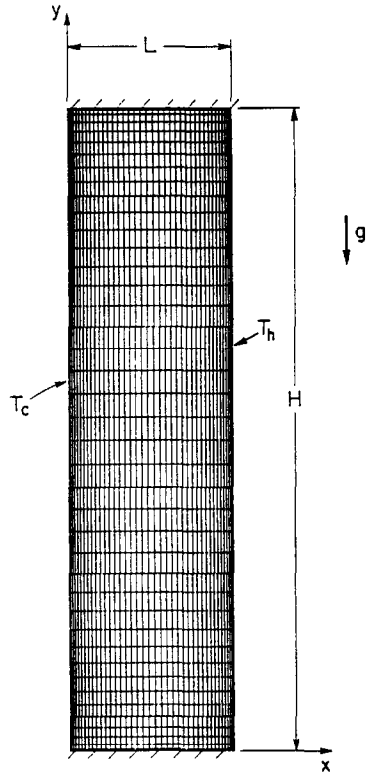

FIG. 1. Schematic of computational domain.

assumption of local thermodynamic equilibrium permits use of the phase diagram to relate mixture and phase compositions, while the assumption of constant density implies a non-deforming solid and a saturated solid–liquid mixture.

Casting the conservation equations and supplementary relations in dimensionless form, it may be shown that the system of interest is characterized by 13 dimensionless parameters. However, the meaning and utility of the parameters is clouded by the absence of true length, temperature, composition and velocity scales. The existence of such scales is precluded by the irregular time-dependent geometry of the three regions and the dependence of solidus and liquidus temperatures on composition.

An elliptic, control-volume-based, finite-difference scheme has been used to solve the continuum equations, and details of the numerical procedure, including discussions of grid and time-step independence, are discussed elsewhere [11, 14]. Results of this study were obtained using a 58×58 grid, biased as shown in Fig. 1. The mold dimensions corresponded to those of the experimental study [12], $H = 144$ mm and $L = 36$ mm, and the cavity was charged with a superheated NH_4Cl–H_2O solution of composition f_o^α and temperature T_o. Solidification was induced at $t = 0$ by reducing the temperature of one vertical surface to a value T_c which is less than the eutectic temperature ($T_e = -15°C$), while maintaining the opposite surface at the initial temperature ($T_h = T_o$). Required thermophysical property data for the NH_4Cl–H_2O system have been presented elsewhere [11]. Calculations were performed on a CDC Cyber 205 supercomputer and required approximately 40 s of CPU time for each second of simulation time.

3. COMPARISON OF PREDICTED AND MEASURED RESULTS

The large CPU time requirements for a complete transient calculation restricted considerations to a single experimental condition, and representative conditions corresponding to experiments 1-2(H) of the companion paper [12] were chosen. Hence, the initial composition and temperature were $f_o^\alpha = 0.30$ and $T_o = 40°C$, and solidification was induced by maintaining wall temperatures of $T_c = -30°C$ and $T_h = 40°C$. Due to uncertainties in measurement of the initial solution concentration, two sets of calculations were performed, one for $f_o^\alpha = 0.30$ and the other for $f_o^\alpha = 0.31$, in order to examine the effect of this uncertainty.

A photographic account of the solidification process for experiment 1-2(H) is shown in Fig. 2. The formation of three distinct regions (pure solid, solid–liquid or mushy, and pure liquid) is indicated. The thin white line has been added to highlight the solidus, which separates the slightly lighter (solid) and darker (mushy) zones. Initially, growth of the mushy region is faster than that of the pure solid, and the liquidus interface appears irregular, indicating a dendritic growth structure (Fig. 2(a)). As solid forms, water enrichment of the adjoining liquid renders it less dense than the bulk liquid, and the solutal buoyancy forces induce an upflow of cold, water-rich fluid through the mushy region to the top of the cavity. As cool, water-rich fluid accumulates at the top of the cavity, a double-diffusive interface is formed, separating the water-rich fluid from underlying fluid which is at nearly the initial composition. Due to the temperature difference across the cavity, there is counterclockwise, thermally driven circulation within each of the two regions. Remelting of solid phase material in the mushy region at the top of the cavity (Fig. 2(b)) occurs due to water enrichment of the adjoining fluid and consequent depression of the liquidus temperature. With increasing time, the double-diffusive interface progresses downward and eventually decomposes, causing merger of the two liquid regions into one well-mixed region. At steady state (Fig. 2(c)) liquid in this region experiences a thermally induced, counterclockwise circulation that gradually smooths the liquidus front.

Comparisons of measured and predicted results are made in terms of solidification morphology (Figs. 3 and 4), liquid mass fraction (Fig. 5), and temperatures (Figs. 6 and 7). Different initial concentrations of $f_o^\alpha = 0.30$ and 0.31 were used in the predictions to assess the effect of uncertainties in knowledge of the actual (experimental) value.

At early times for $f_o^\alpha = 0.30$ predicted solidus and

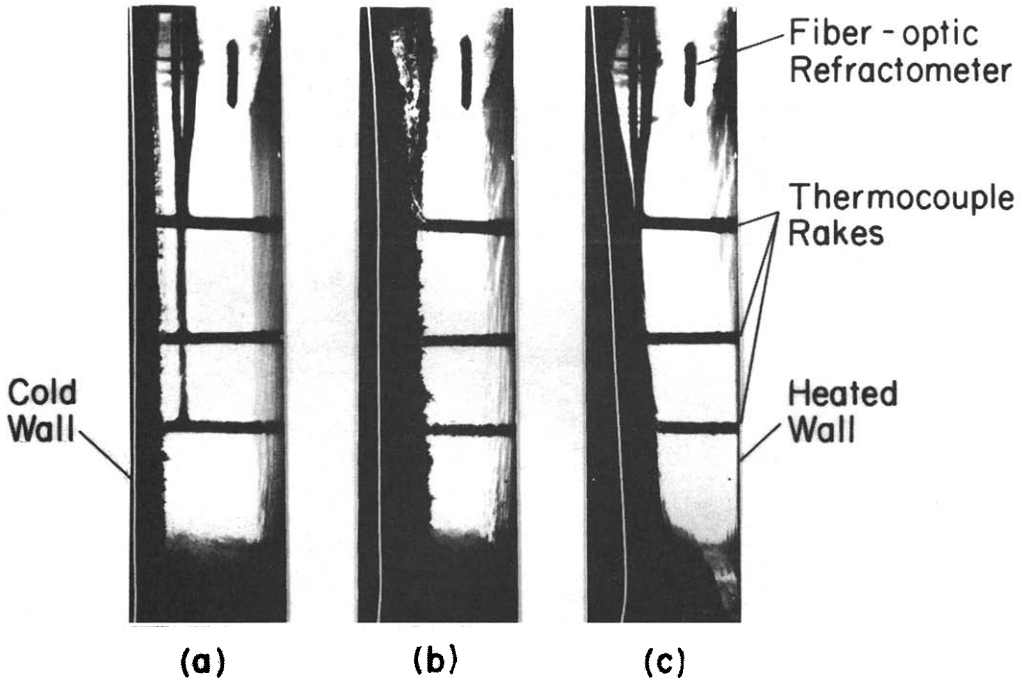

FIG. 2. Experimental solidification morphology at: (a) 3 min; (b) 11 min; (c) 56 min (steady state).

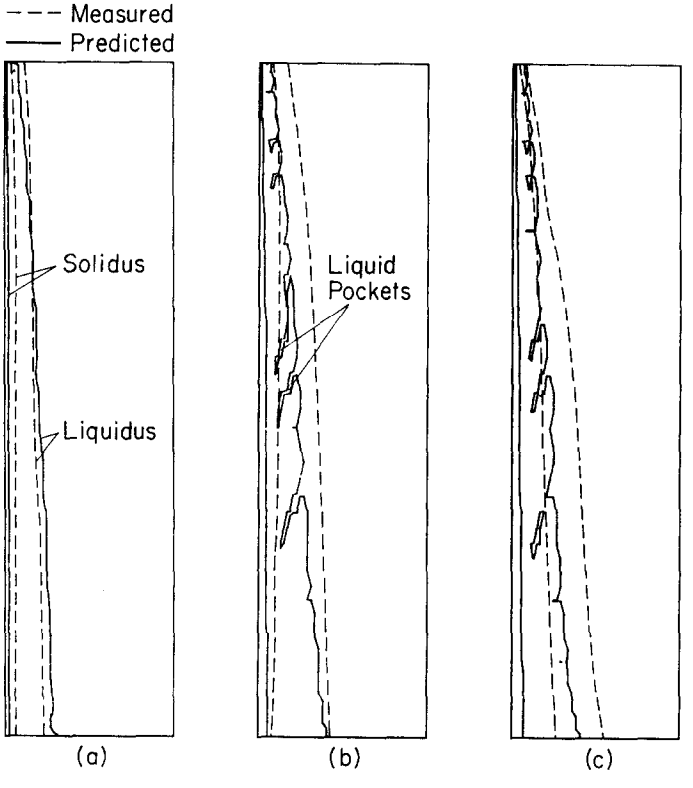

FIG. 3. Measured and predicted ($f_o^a = 0.30$) interface locations at: (a) 3 min; (b) 11 min; (c) 20 min.

liquidus fronts are in reasonable agreement with the experimental results. With increasing time, however, differences become more pronounced and actual development of the fronts is underpredicted by the model. Moreover, a final steady-state condition is predicted to occur at $t \approx 20$ min, while, experimentally, it is observed to occur at $t \approx 56$ min (Fig. 2). At the respective steady states, solidification is underpredicted by approximately 60 and 25% for the solid and mushy regions, respectively. However, the model is successful in predicting the observed liquidus front irregularities (Figs. 2(a) and (b)), as well as the retar-

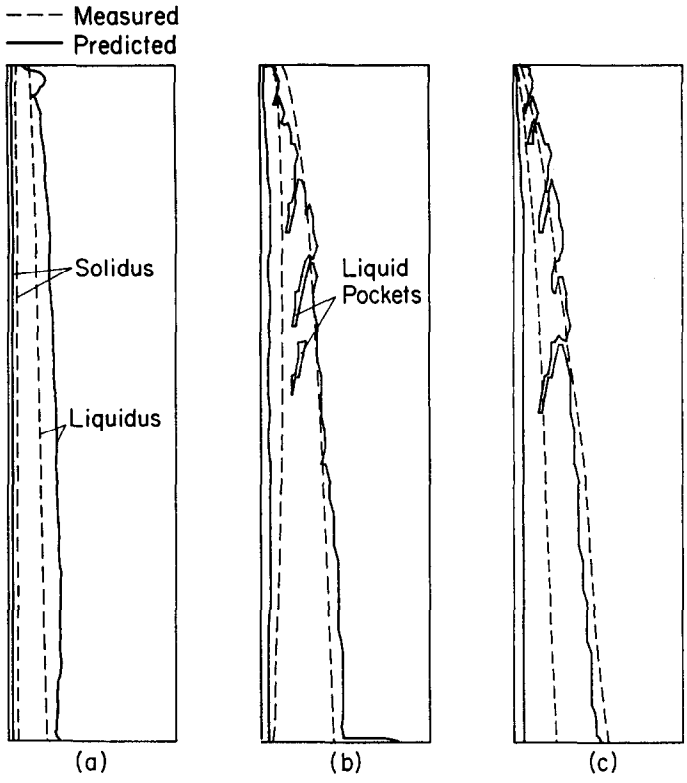

FIG. 4. Measured and predicted ($f_o^\alpha = 0.31$) interface locations at: (a) 3 min; (b) 11 min; (c) 15 min.

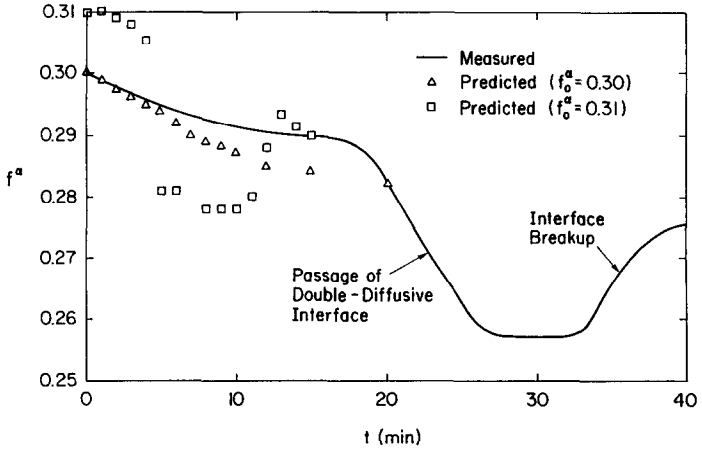

FIG. 5. Measured and predicted liquid mass fraction at $x = 27$ mm, $y = 135$ mm, $z = 0$ mm.

dation of liquidus growth at the top of the cavity. Retardation is due to an accumulation of water-rich fluid and to the incidence of warm fluid from the thermally driven flow.

With respect to prediction of the liquidus front at later times, there is much better agreement with the data when the predictions are based on $f_o^\alpha = 0.31$ (Figs. 4(b) and (c)). However, growth of the solid region is again underpredicted by approximately 60%, and steady state is predicted to occur at $t \approx 15$ min in contrast to the experimental value of $t \approx 56$ min. The predicted results of Figs. 3(b), (c) and 4(b), (c) reveal the existence of deep pockets of liquid within the mushy region. The pockets are channels which form due to remelting caused by the flow of water-rich fluid within the mushy region. As the channels develop, they provide preferred paths for the flow of interdendritic fluid and lead to a pattern of solute redistribution known as A-type macrosegregation. While such channels could not be observed experimentally under normal lighting conditions, traces of their existence were observed under intense lighting. The existence of such channels has been observed by other investigators [4, 15, 16].

The variation with time of the predicted and measured mass fraction of NH_4Cl at a fixed point within

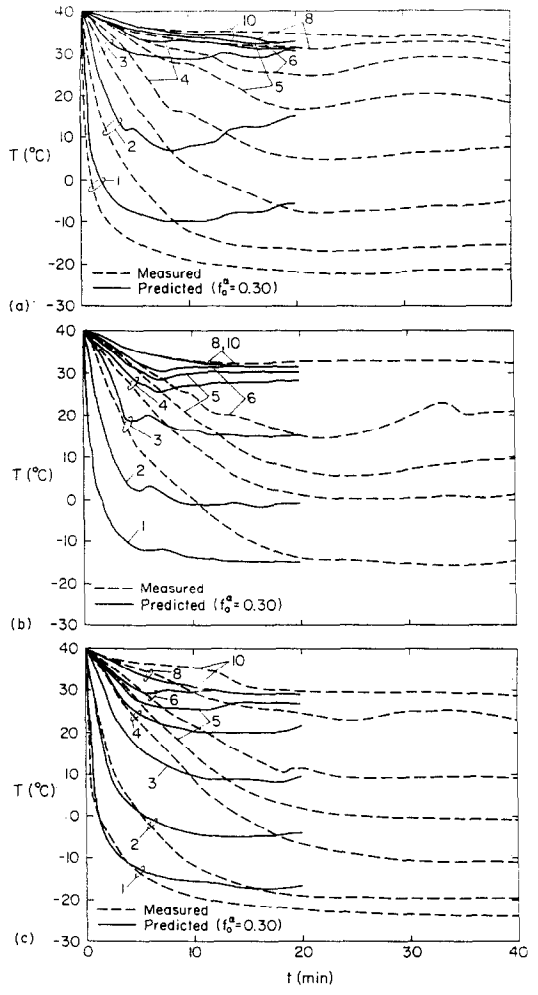

FIG. 6. Measured and predicted ($f_o^z = 0.30$) temperature histories for selected x locations at: (a) $u = 90$ mm; (b) $y = 65$ mm; (c) $y = 45$ mm.

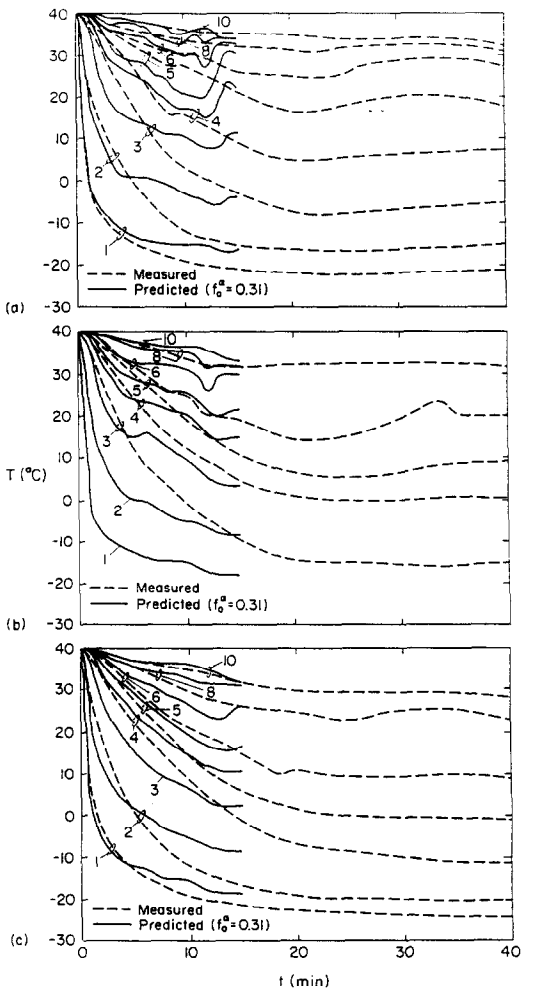

FIG. 7. Measured and predicted ($f_o^z = 0.31$) temperature histories for selected x locations at: (a) $y = 90$ mm; (b) $y = 65$ mm; (c) $y = 45$ mm.

the liquid is shown in Fig. 5. The initial decrease in concentration which is both predicted and measured is due to the rejection of water-rich fluid from the mushy region into the melt. The measurements reveal a more pronounced reduction in concentration over the time interval $20 \lesssim t \lesssim 26$ min, which is followed by a significant increase for $t \gtrsim 32$ min. Respectively, the reduction and increase are due to downward movement of the double-diffusive interface past the measurement location and erosion or break-up of the interface. From the start of the experiment to steady-state conditions, the measurements reveal an overall reduction in the liquid mass fraction of $\Delta f^{NH_4Cl} \approx -0.025$. Although the significant changes in f^{NH_4Cl} which result from interface passage and erosion are not predicted for $f_o^{NH_4Cl} = 0.30$, they are predicted for $f_o^{NH_4Cl} = 0.31$. For the slightly larger concentration, solidification rates and attendant water rejection are large enough to result in formation and downward propagation of a single double-diffusive interface, thereby facilitating prediction of the sharp changes in f^{NH_4Cl}, although at much smaller times. For $f_o^{NH_4Cl} = 0.31$, the predicted overall change in the mass fraction is $\Delta f^{NH_4Cl} \approx -0.02$.

Measured temperature histories at selected locations within the cavity are contrasted with results predicted for $f_o^{NH_4Cl} = 0.30$ in Fig. 6. Predicted and measured results correspond to three vertical stations ($y = 45$, 65 and 90 mm) and, for each station, to distances of $x = 2.2$, 4.4, 6.6, 8.7, 10.9, 13.1, 17.5, and 26.2 mm from the cold wall (thermocouple numbers 1, 2, 3, 4, 5, 6, 8, 10 of ref. [12]). Good agreement is restricted to locations near the hot wall (thermocouples 8, 10) and to locations near the cold wall (thermocouples 1, 2) at early times ($t \lesssim 5$ min). Disagreement is most pronounced at locations near the solidus and liquidus interfaces and increases with increasing time. At these locations predicted temperatures exceed the data by 10–30°C.

Improved agreement between the predictions and measurements is obtained when the predictions are based on an initial composition of $f_o^{NH_4Cl} = 0.31$ (Fig.

7). At most locations predictions are within 5°C of the measurements for $t \leqslant 12$ min. At $t \approx 12$ min, decomposition of the double-diffusive interface is predicted to occur, causing large excursions in the predicted temperatures. At steady state predicted temperatures exceed the data by 5–20°C. Achievement of better accuracy is limited by the inability to precisely determine solidus and liquidus interface locations (Fig. 4).

The foregoing comparisons reveal that, despite recent progress in model development for binary solidification, it is still difficult to obtain quantitative agreement with experimental results. Discrepancies are attributed to weaknesses in the model assumptions, with the most likely candidates involving departures from laminar flow and local thermodynamic equilibrium, anisotropies in the mushy region permeability, and non-constant properties. For example, opposing solutal and thermal buoyancy forces at the liquidus interface, as well as the irregular nature of the interface, can induce turbulence in the adjoining flow. In addition, heat release and water rejection during solidification provide sources of thermal and chemical nonequilibrium, respectively, within the mushy region. Dendritic solidification renders the assumption of isotropic permeability highly suspect, and properties do vary with composition, as well as temperature. The property data base itself may be highly uncertain, as, e.g. in knowledge of the constant K_o appearing in equation (13) and the validity of the equation itself.

Although quantitative agreement between the predictions and the data is limited, predictions based on an initial composition of $f_o^\alpha = 0.31$ have yielded important trends which were observed experimentally. To expand upon these trends, predicted velocity, temperature and composition fields are plotted at five times during the solidification process (Figs. 8–12). The solidus and liquidus interfaces are highlighted on the velocity vector plots, while streamlines are plotted in increments of $\psi_{max,1}/9$ for the bulk liquid and $\psi_{max,s+l}/4$ for the mushy region. Isotherms are plotted in increments of $(T_h - T_c)/20$, and isocomposition lines are plotted in increments of $(f_o^\alpha - f_e^\alpha)/20$, where the eutectic composition f_e^α is associated with the solidus line.

Conditions at $t = 1$ min are shown in Fig. 8. Growth of both the solid and mushy regions is nearly planar, with the mushy region growing at a much faster rate. The bulk liquid remains at a nearly uniform temperature and composition, and flow is primarily characterized by a thermally driven counterclockwise circulation. The effects of solutal buoyancy, however, are already evident at the top of the cavity. The outflow of water-rich interdendritic fluids into the bulk liquid is indicated by the streamlines of Fig. 8(b). A weak, clockwise circulation exists, linking the flow of fluid in the mushy and liquid regions. The isotherms and isocomposition lines of Figs. 8(c) and (d) confirm that cool, water-rich fluid begins to accumulate at the top of the cavity.

By $t = 5$ min, a recirculating zone is well established at the top of the cavity (Fig. 9(b)). The flow, which is dominated by thermal buoyancy, is counterclockwise, as fluid ascends in a thermal boundary layer along the hot wall and descends along the cooler liquidus front (Fig. 9(c)). Average values of the liquid temperature and NH_4Cl composition (Fig. 9(d)) are smaller than values (T_o and f_o^α) associated with the initial state. Conditions within the bulk liquid have clearly become double-diffusive in the sense that a stable density interface separates colder, solute-deficient fluid in a top convection layer from warmer, solute-rich fluid in an underlying layer. Remelting within the mushy zone adjoining the top layer is evident (Fig. 9(a)) and results from a liquidus temperature depression due to water enrichment of the top layer and the incidence of the fluid from the hot side wall. The streamlines (Fig. 9(b)) also indicate a flow of water-rich interdendritic fluid to and from the bulk liquid just below the double-diffusive interface, and within the mushy region associated with the streamlines, channels have begun to form.

Due to sustained flow of water-rich fluid into the top layer, the double-diffusive interface descends with increasing time (Fig. 10), as remelting continues at the top of the mushy region and channels within the mush become more prominent. However, for $t > 8$ min, the flow of interdendritic fluids into the top layer is greatly diminished, top layer growth is arrested, and the diffusive interface is eroded by the recirculating flows in the adjoining convection layers. At $t = 12$ min (Fig. 11), the interface has been broken, and there is no longer a prominent recirculating fluid layer at the top of the cavity. The top and bottom fluid layers become mixed, as a single recirculation zone begins to establish itself over the entire height of the cavity. Solidification has virtually ceased, but remelting continues in upper portions of the mushy region (Fig. 11(a)). The irregular isotherms (Fig. 11(c)) and isocomposition lines (Fig. 11(d)) in the bulk liquid region are indicative of the mixing which is occurring.

At steady state ($t = 15$ min, Fig. 12), a single recirculating zone has established itself in the bulk liquid. The counterclockwise fluid motion is thermally driven (Fig. 12(b)), and the bulk liquid is once again characterized by a uniform composition (Fig. 12(d)), but one which is less than the original value of $f_o^\alpha = 0.31$. The liquid is thermally stratified (Fig. 12(c)), as in the case of a cavity with differentially heated sidewalls and no solidification. The channels remain in the mushy region, where there is no further remelting of the solid phase.

4. SUMMARY

Predicted and experimental results have been compared for solidification of a binary NH_4Cl–H_2O mixture in a rectangular cavity. Using a newly developed

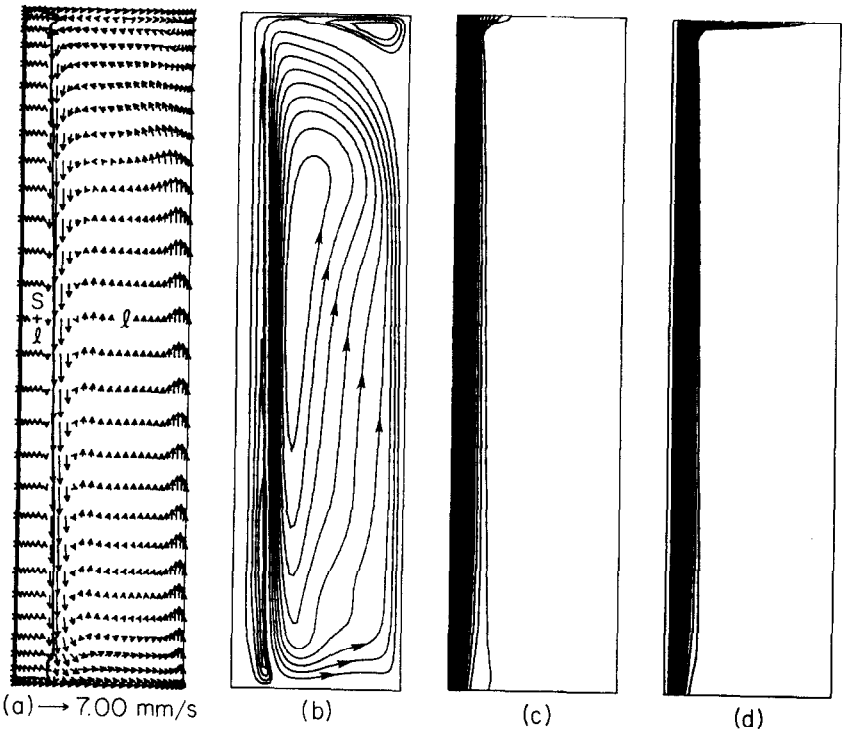

FIG. 8. Solidification behavior at $t = 1$ min for $f_0^\alpha = 0.31$: (a) velocity vectors; (b) streamlines ($\psi_{max,l} = 2.56 \times 10^{-2}$, $|\psi_{max,s+l}| = 8.88 \times 10^{-4}$); (c) isotherms; (d) isocomposition lines ($f^\alpha_{l,max} = 0.31$).

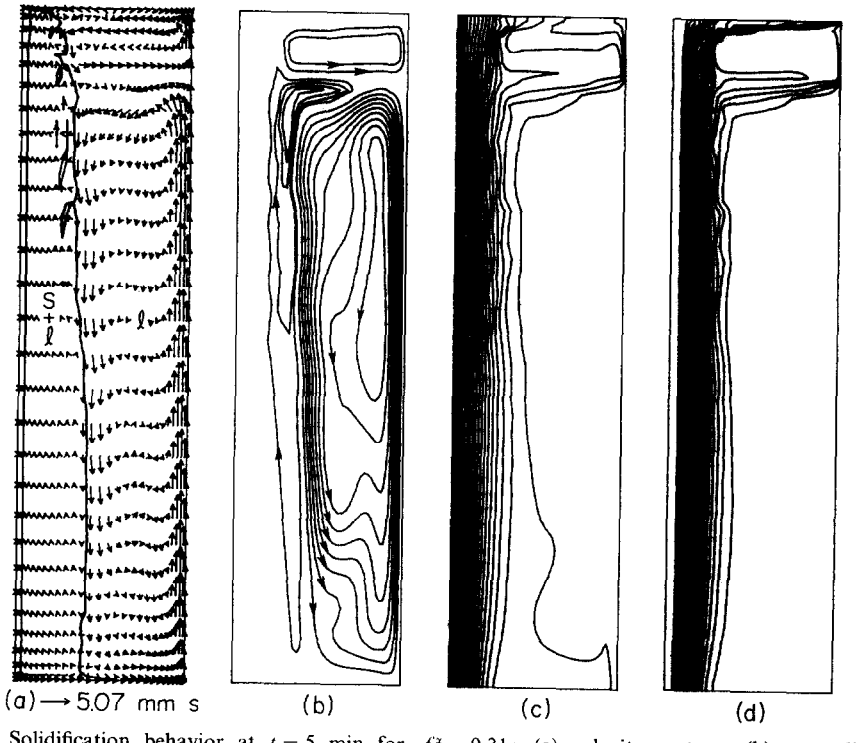

FIG. 9. Solidification behavior at $t = 5$ min for $f_0^\alpha = 0.31$: (a) velocity vectors; (b) streamlines ($\psi_{max,l} = 1.81 \times 10^{-2}$, $|\psi_{max,s+l}| = 2.64 \times 10^{-3}$); (c) isotherms; (d) isocomposition lines ($f^\alpha_{l,max} = 0.309$).

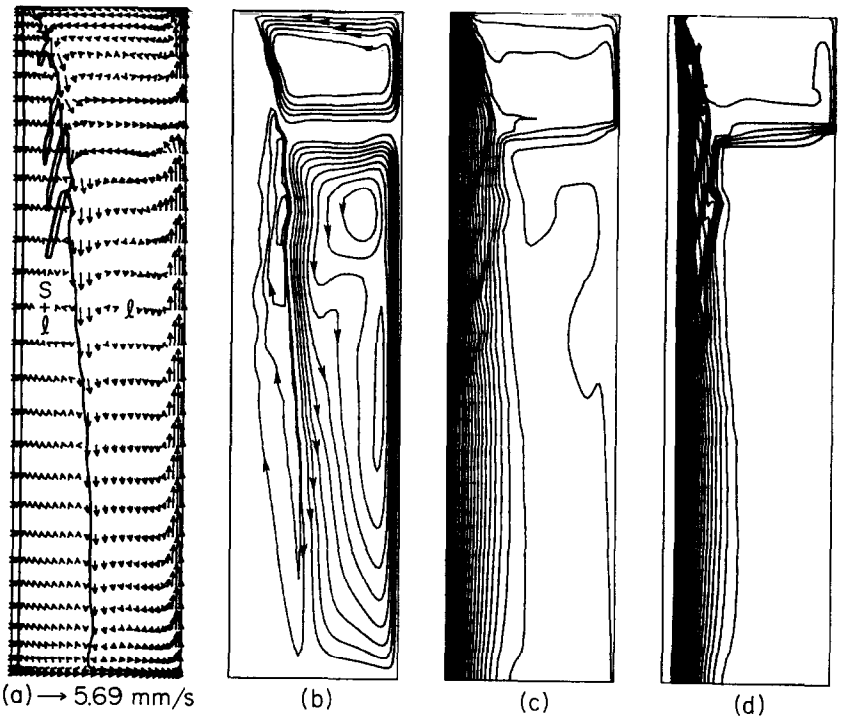

FIG. 10. Solidification behavior at $t = 8$ min for $f_o^\alpha = 0.31$: (a) velocity vectors; (b) streamlines ($\psi_{max,l} = 1.68 \times 10^{-2}$, $|\psi_{max,s+l}| = 1.14 \times 10^{-3}$); (c) isotherms; (d) isocomposition lines ($f_{l,max}^\alpha = 0.304$).

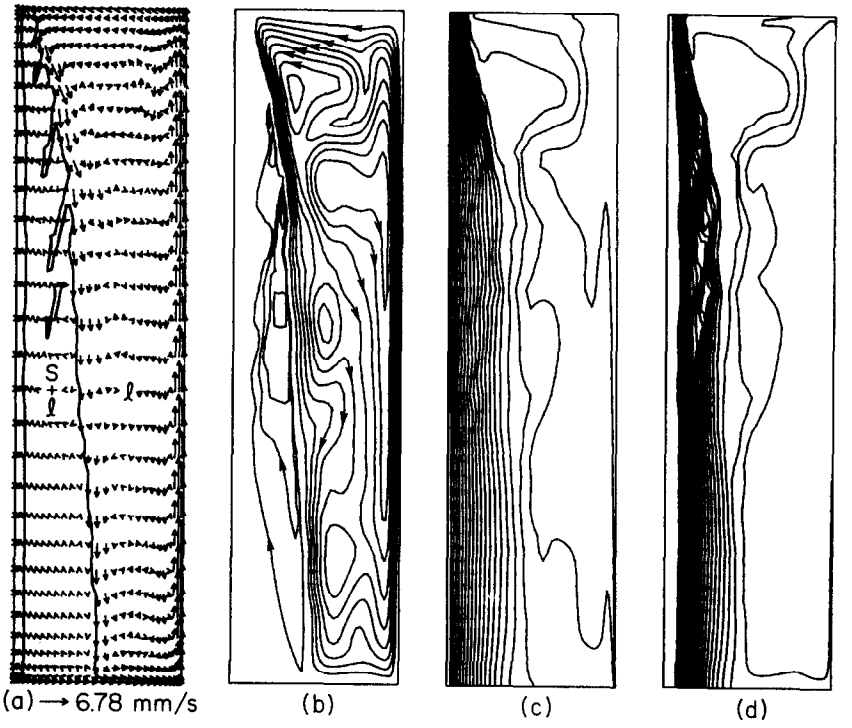

FIG. 11. Solidification behavior at $t = 12$ min for $f_o^\alpha = 0.31$: (a) velocity vectors; (b) streamlines ($\psi_{max,l} = 1.58 \times 10^{-2}$, $|\psi_{max,s+l}| = 5.19 \times 10^{-4}$); (c) isotherms; (d) isocomposition lines ($f_{l,max}^\alpha = 0.299$).

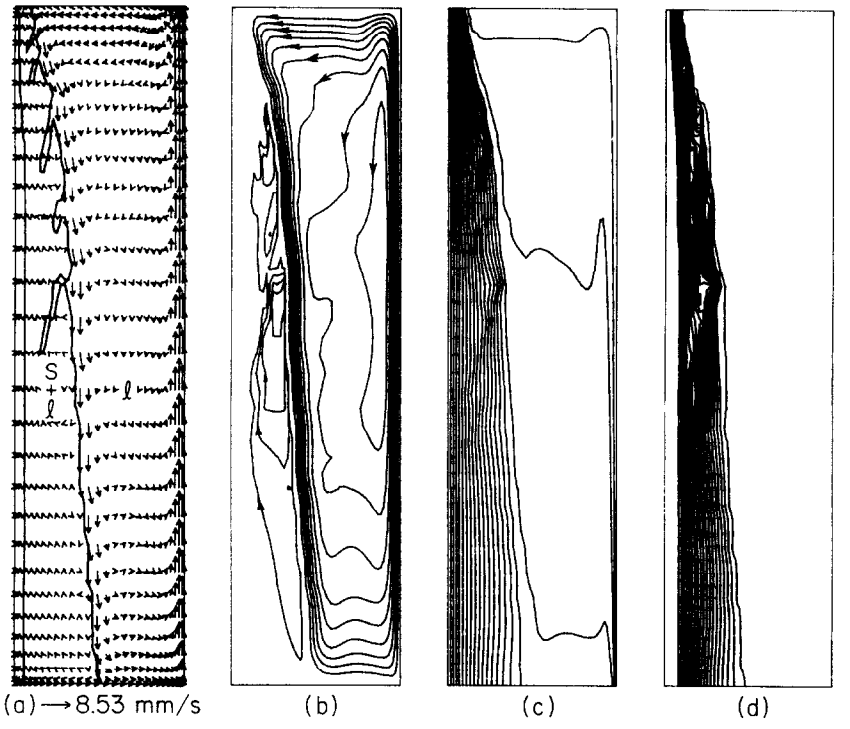

FIG. 12. Solidification behavior at $t = 15$ min for $f_o^\alpha = 0.31$: (a) velocity vectors; (b) streamlines ($\psi_{max,l} = 2.08 \times 10^{-2}$, $|\psi_{max,s+l}| = 3.26 \times 10^{-4}$); (c) isotherms; (d) isocomposition lines ($f_{l,max}^\alpha = 0.296$).

continuum model, two sets of transient calculations were performed for two slightly different initial NH_4Cl concentrations, and comparisons with experiment were based on the solidus and liquidus interface locations, the liquid NH_4Cl composition at a particular location, and temperatures at many locations throughout the cavity.

Qualitatively, several important features of the solidification process were predicted by the model. In particular, the prediction of irregularities in the liquidus front, as well as the retardation of front growth at the top of the cavity due to remelting and impingement of a thermally driven flow, compared favorably with the experimental results. Also, the prediction of channeling in the mushy region due to the flow of water-rich interdendritic fluids was consistent with experimental observations. However, the ability to predict other experimental features depended strongly on the initial composition used for the calculations.

The two sets of calculations differed greatly according to whether the initial mass fraction of NH_4Cl was set at 0.30 or 0.31, thereby indicating a strong dependence of solidification on the initial composition. For $f_o^\alpha = 0.30$, no double-diffusive layering was predicted, and the agreement with experimental results, which were strongly influenced by double-diffusive effects, was poor. However, when the initial composition was increased by only 1%, the model was able to predict experimental observations associated with the formation, propagation and breakup of a single double-diffusive interface. In addition, there was reasonable agreement between predictions and measurements for the liquidus interface locations and for temperature and liquid composition changes. However, predicted times for the occurrence of major events, such as those associated with double-diffusive layering, were much less than the measured times and the extent of solid region growth was significantly underpredicted. Although the specific source(s) of the discrepancies could not be confirmed, likely candidates are associated with model assumptions and an uncertain property data base. Knowledge of the permeability, including the effect of anisotropies and state variables such as temperature and solid mass fraction, is particularly suspect.

The results of this study have confirmed that the continuum model is able to predict key features of binary solidification which include liquidus front irregularities and effects of solute rejection such as remelting and double-diffusive layering. However, solidification in binary substances is characterized by a broad spectrum of complex processes, and even with a reliable property data base, model improvements may be needed to achieve precise quantitative agreement with experimental results. The specific nature of such improvements will depend on gaining an improved understanding of the extent to which solidification is influenced by effects such as turbulence, nonequilibrium and variable properties.

Acknowledgement—Support of this work by the U.S. Department of Energy (Office of Basic Energy Sciences)

under Grant No. DE-FG02-87ER13759 is gratefully acknowledged.

REFERENCES

1. M. C. Flemings and G. E. Nereo, Macrosegregation: Part I, *Trans. Metall. Soc. A.I.M.E.* **239,** 1449–1461 (1967).
2. M. C. Flemings, R. Mehrabian and G. E. Nereo, Macrosegregation: Part II, *Trans. Metall. Soc. A.I.M.E.* **242,** 41–49 (1968).
3. M. C. Flemings and G. E. Nereo, Macrosegregation: Part III, *Trans. Metall. Soc. A.I.M.E.* **242,** 50–55 (1968).
4. R. Mehrabian, M. Keane and M. C. Flemings, Interdendritic fluid flow and macrosegregation: influence of gravity, *Met. Trans.* **1,** 1209–1220 (1970).
5. S. Kou, D. R. Poirier and M. C. Flemings, Macrosegregation in rotated remelted ingots, *Met. Trans. B* **9B,** 711–719 (1978).
6. T. Fujii, D. R. Poirier and M. C. Flemings, Macrosegregation in a multicomponent low alloy steel, *Met. Trans. B* **10B,** 331–339 (1979).
7. S. D. Ridder, S. Kou and R. Mehrabian, Effect of fluid flow on macrosegregation in axi-symmetric ingots, *Met. Trans. B* **12B,** 435–447 (1981).
8. J. Szekely and A. S. Jassal, An experimental and analytical study of the solidification of a binary dendritic system, *Met. Trans. B* **9B,** 389–398 (1978).
9. M. E. Thompson and J. Szekely, Mathematical and physical modeling of double-diffusive convection of aqueous solutions crystallizing at a vertical wall, *J. Fluid Mech.* **187,** 409–433 (1988).
10. W. D. Bennon and F. P. Incropera, A continuum model for momentum, heat and species transport in binary solid–liquid phase change systems—I. Model formulation, *Int. J. Heat Mass Transfer* **30,** 2161–2170 (1987).
11. W. D. Bennon and F. P. Incropera, A continuum model for momentum, heat and species transport in binary solid–liquid phase change systems—II. Application to solidification in a rectangular cavity, *Int. J. Heat Mass Transfer* **30,** 2171–2187 (1987).
12. M. S. Christenson and F. P. Incropera, Solidification of an aqueous ammonium chloride solution in a rectangular cavity—I. Experimental study, *Int. J. Heat Mass Transfer* **32,** 47–68 (1989).
13. S. Asai and I. Muchi, Theoretical analysis and model experiments on the formation mechanism of channel-type segregation, *Trans. ISIJ* **18,** 90–98 (1978).
14. W. D. Bennon and F. P. Incropera, Numerical analysis of binary solid–liquid phase change using a continuum model, *Numer. Heat Transfer*, to be published.
15. R. J. McDonald and J. D. Hunt, Fluid motion through the partially solid regions of a casting and its importance in understanding A type segregation, *Trans. Metall. Soc. A.I.M.E.* **245,** 1993–1997 (1969).
16. A. Sample and A. Hellawell, The effect of mold precision on channel and macrosegregation in ammonium chloride–water analog castings, *Met. Trans. B* **13B,** 495–501 (1982).

SOLIDIFICATION D'UNE SOLUTION AQUEUSE DE CHLORURE D'AMMONIUM DANS UNE CAVITE RECTANGULAIRE—II. COMPARAISON DES RESULTATS DU CALCUL ET DES EXPERIENCES

Résumé—Des comparaisons entre des résultats expérimentaux et numériques pour la solidification d'une solution binaire NH_4Cl–H_2O dans une cavité rectangulaire sont faites pour un nouveau modèle continu. Celui-ci prédit les points principaux du mécanisme de solidification tels que les irrégularités à l'interface du liquidus, la refusion, le développement et l'érosion ultérieure d'un interface doublement diffusif. Néanmoins, à cause d'incertitudes sur les propriétés et à cause des limitations des hypothèses faites dans le modèle, un bon accord quantitatif ne peut être obtenu pour tous les cas expérimentaux.

DER ERSTARRUNGSPROZESS EINER WASSERHALTIGEN AMMONIUMCHLORIDLÖSUNG IN EINEM RECHTECKIGEN HOHLRAUM—II. VERGLEICH VON BERECHNETEN UND GEMESSENEN ERGEBNISSEN

Zusammenfassung—Experimentelle und numerische Ergebnisse für den Erstarrungsvorgang einer binären NH_4Cl–H_2O-Lösung in einem rechteckigen Hohlraum werden verglichen. Das neu entwickelte Kontinuumsmodell ermöglicht eine Vorhersage der Hauptmerkmale des Erstarrungsprozesses, wie z. B. Unregelmäßigkeiten der Liquidus-Grenzfläche, Wiederaufschmelzen sowie Entstehung und Abbau einer Grenzfläche mit temperatur- und konzentrationsgetriebener Strömung. Durch die Ungenauigkeiten der vorhandenen Stoffdaten und/oder Begrenzungen der entsprechenden Annahmen im Modell kann jedoch nicht für alle Datensätze gute quantitative Übereinstimmung erreicht werden.

ЗАТВЕРДЕВАНИЕ ВОДНОГО РАСТВОРА ХЛОРИДА АММОНИЯ В ПРЯМОУГОЛЬНОЙ ПОЛОСТИ—II. СРАВНЕНИЕ РАСЧЕТОВ С РЕЗУЛЬТАТАМИ ИЗМЕРЕНИЙ

Аннотация—При помощи новой модели сплошной среды проведено сравнение экспериментальных и численных результатов по затвердеванию бинарного раствора NH_4Cl–H_2O в прямоугольной полости. Модель определяет такие основные характеристики процесса затвердевания, как неровность границы ликвидуса, повторное плавление, а также развитие и последующую эрозию двойной диффузионной границы. Однако вследствие неопределенностей в имеющихся исходных данных и ограничений, заложенных в модель, не получено хорошего количественного соответствия для всех характеристик.